Jams and Cakes: A Closer Look on Well Clogging Mechanisms in Microscale Produced Water ReInjection Experiments

Aurélie Le Beulze, Nathalie Santos De Pera, Bertrand Levaché, Mathias Questel, Pascal Panizza, François Lequeux, Michael Levant, Nicolas Passade-Boupat

Jams and cakes: a closer look on well clogging mechanisms in microscale Produced Water Re-Injection experiments

Aurélie Le Beulze[1,5] • Nathalie Santos De Pera[3,4,5] • Bertrand Levaché[2] • Mathias Questel[3] • Pascal Panizza[4,6] • François Lequeux[4,5] • Michael Levant[3,5] • Nicolas Passade-Boupat[3,5]

Abstract

We present a new experimental approach to further understand the injectivity impairment due to reinjection of produced water in an oilfield, containing residual oil and solids. A unique microfluidic setup with imposed flowrate is characterized by excellent reproducibility and allows one to determine the kinetics of external cake formation and the propagation of the damage inside the porous medium, similar to what happens at the injection wellbore. The growth rates of the external cake and that of the propagation of the internal damage exhibit discontinuities, likely related to a pressure buildup up to a threshold Laplace pressure above which the O/W Pickering droplets are pushed through, and which sets a limit to the cake growth. Finally, the external cake reaches a quasi-stationary thickness whose mechanisms are discussed below. Direct visualization readily achieved in microfluidic experiments, coupled with spatiotemporal image analysis, enable better spatial resolution than core flooding experiments, and show that the damage occurs in a small region close to the entry to the porous medium. These developments lead to the derivation of an analytical model of the damage formation. It appears that although very localized, this damage strongly decreases the global permeability of the whole porous medium. Finally, controlled temperature experiments permit to identify the variation of the viscosity of the oil droplets (or the viscosity ratio), as the primary mechanism by which temperature influences clogging. Clogging is slowed at high temperatures, but the final state is characterized by particle clogging and is thus irreversible.

Article Highlights

- **Novel method to study PWRI, comprising a microfluidic setup with direct visualization, coupled with image analysis**
- **Analytical model derived for the damage propagation and the permeability decline during PWRI experiments with 3 different regions.**
- **Temperature impacts the clogging through variation of viscosity, with a qualitatively different final jammed state.**

Keywords clogging · produced water · porous media · injectivity decline · Pickering emulsions

---

★ Nathalie Santos De Pera ; Michael Levant
nathalie.santos-de-pera [at] totalenergies.com ; michael.levant [at] totalenergies.com

[1] Laboratoire Sciences et Ingénierie de la Matière Molle, ESPCI Paris, CNRS, PSL University, Sorbonne Université, 75005 Paris, France; Current : UGIEL, 87 Avenue du Docteur Albert Schweitzer, 33600 Pessac, France

[2] TotalEnergies SE, Centre de Recherche Feluy, Zoning industriel, Zone C, 7181 Feluy, Belgium

[3] TotalEnergies SE, Pôle d'Études et Recherche de Lacq, BP 47, 64170 Lacq, France

[4] Laboratoire Science et Ingénierie de la Matière Molle, ESPCI Paris, PSL University, Sorbonne Université, CNRS, F-75005 Paris, France

[5] Laboratoire Physico-Chimie des Interfaces Complexes, Bâtiment CHEMSTARTUP, Route départemental 817, 64170 Lacq, France.

[6] Institut de Physique de Rennes (UMR CNRS 6251), 263 Av. du général Leclerc, Campus Beaulieu, Université Rennes 1, 35042 Rennes.

1. Introduction

Water management in an oilfield is both a technical and environmental challenge (Abou-Sayed et al., 2007). The amount of Basic Sediment and Water (BS&W) can reach 80% or even higher (Khatib and Verbeek, 2003). On the other end, water injection is often needed to optimize oil production by maintaining the reservoir pressure. A way to recycle this produced water is to re-inject it via injection wells: produced water re-injection (PWRI) will allow to reduce water uptake in the environment. The complexity of developing this process in an oil field has been quickly identified, especially the determination of water quality specifications (Evans, 1994): whereas produced water discharge specifications are mainly based on "macroscopic" quantities (oil, solids) allowed, PWRI specifications will also be sensitive to more "microscopic" characteristics. This method often leads to formation damage causing injectivity loss, technical issues, and budgetary repercussions. Injectivity decline represents a significant problem for well performance and the necessity to preserve a specified injection rate was shown in a case study (Sharma and Pang, 2000).

Formation damage is due to the residual oil and solids particles contained in the produced water, represented schematically in **Fig.1a**. Clogging phenomena can occur during transport of suspensions, such as oil droplets and/or solids, through a porous medium, causing decrease of the flow rate. Several mechanisms can induce clog formation depending on the properties of the suspension and of the porous medium. However, these mechanisms are not fully understood and have been a subject of research made on different length scales, as described below.

Studies at a pore scale in microfluidics have allowed one to identify the microscopic physical mechanisms at play for clogging by solid particles. For example, sieving happens when a particle is larger than a constriction, but even if the particle size is smaller, clog formation is possible by bridging or successive deposition depending on surface chemistry and charges (Delouche et al., 2020; Dressaire and Sauret, 2017; Sauret et al., 2018). Most of the studies deal with clogging with particles only. The presence of other species adds further complexity: surfactant molecules or the simultaneous presence of oil droplets and solids particles (Pickering emulsion) can affect clogging by modifying the passage times of the particle/surfactant laden drop through the contraction (De Soete et al., 2021). Thus, the advantage of microfluidics relies on the direct visualization of the phenomena at play that is useful to understand the behavior of one drop or particle in one contraction.

More generally in the colloidal field, many studies have focused on injectivity impairment and damage formation. Scientists have visualized suspension transport in homogeneous patterns of pore networks to define parameters influencing particle capture: pore size distribution, pore roughness or ionic strength have been considered (Agbangla et al., 2012; Auset and Keller, 2006; Wyss et al., 2006). Others have used filter media to characterize filter cake formation: conditions and rate of cake building up could then be determined and models predicting the kinetics of cake thickness and flow rate loss have been established (Jiao and Sharma, 1993). Behavior of oily filter cakes can also depend on filtration pressure, size ratio between pore and droplets and its ability of deformation (Headen et al., 2006). The intricacy of well injectivity impact is illustrated by the large number of physicochemical variables that have been discovered in clogging mechanisms. (Buret et al., 2008, 2010).

Moreover, experimental studies have been conducted on a larger scale with flooding experiments in cores. Researchers have also noted several parameters that can affect well injectivity and induce formation damage. Thus, the effects of the size distributions of the suspension and of the porous media have been investigated and a mathematical model has been developed to describe a random statistical process of particle transport in these porous media (Donaldson et al., 1977). One issue for these model developments in coreflood is the large distance (several centimeters at least) between the different pressure sensors used to measure the impairment evolution. Other studies confirm that, the larger the droplet diameter is, the more severe the formation damage can be (Azizov et al., 2021). The influence of the suspension concentration has also been studied and when oil droplets and particles are both present in the suspension, a significant permeability decline occurs (Zhang et al., 1993). Some studies claim that the size of droplets has a weaker

impact on injectivity decline than that of suspensions containing oil and particles that are known to lead to severe permeability damages (Ali et al., 2007). Such macroscale phenomena could be explained with recent results obtained in microfluidics studies (De Soete, 2021).

Connecting results obtained on different scales is crucial to reach a better understanding of the injectivity decline, however such studies are still scarce (Pang and Sharma, 1997; Rossini et al., 2020) and experiments conducted at a mesoscopic scale in disordered porous media that would link the two length scales are needed.

To bridge that gap, we present in this paper a microscale setup that mimics produced water reinjection on a larger scale (field or core flooding experiments) and enables the study of the evolution of effective permeability to water in a porous medium, representative of an injection wellbore. By coupling permeability measurements with direct observations, it then becomes possible to understand the underlying mechanisms responsible for impairment. An in-house spatiotemporal analysis implemented in MATLAB allows one to follow the formation kinetics of the external cake and of its propagation inside the porous medium. Based on our experimental findings, we derive a simple hydrodynamic model that could offer a reliable framework for large-scale experiments. This model highlights the formation of a very thin region of low permeability responsible for a major part of the average permeability loss of the whole porous medium.

2. Materials and Methods

Details of the specification of equipment and chemical used can be found in the supplementary material. For all the experiments reported herein, the carrier fluid used is a brine with a salinity of 67 g/L, (and 71 g/L for the high temperature experiments). We first use this brine to fill the porous medium and experimentally determine its initial permeability k_0 evaluated in section 2.2. We also use it as a continuous phase for the preparation of the synthetic produced water so that all the injected fluids will have the same ionic strength. The brine composition is as detailed in **Table 1**. After salt addition in water, brine is filtered with a 0.22-µm Millipore membrane. This complex brine composition is intended to mimic complex composition encountered in field operations.

Table 1. Composition of brine used for synthetic produced water at 67 g/L.

Component	**Concentration (ppm)**
Filtered distilled water	
NaCl	59 934
CaCl2	6 188
MgCl2	5 321
KCl	580
NaN3 *(bacterial growth prevention)*	200

2.1. Synthetic produced water

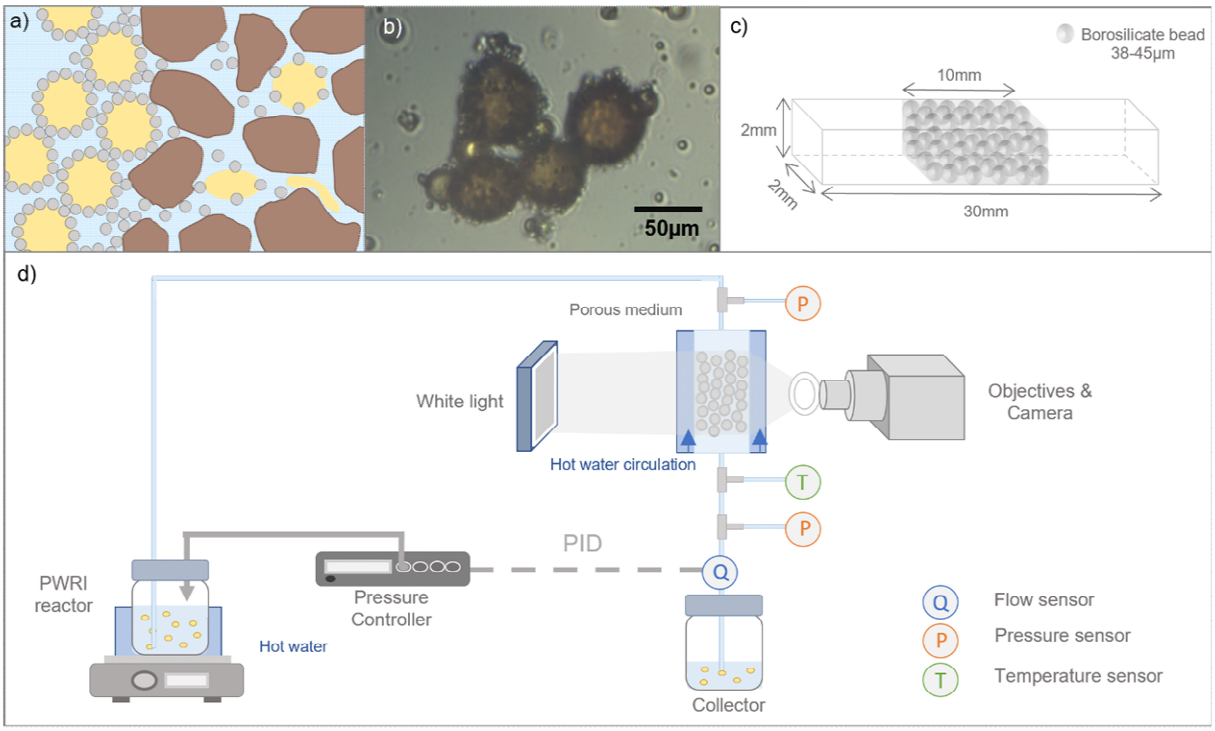

Fig. 1. a) Schema of porous medium clogging caused by solid particles and oil **b)** Photo of O/W Pickering emulsion in produced water; **c)** schema of the porous media **d)** Illustration of the experimental setup.

The synthetic produced water in **Fig.1b** is a dispersion of 200 ppm of crude oil (characteristics detailed in **Table 2** from a field in Africa and 100 ppm of quartz particles (BCR066 from Sigma-Aldrich, <d50> = 1.8 µm) in brine as a continuous phase. The sizes of silica particles used in this study have been determined by granulometry on a Mastersizer 2000 from Malvern. The sealed flask containing the produced water is immersed in an ultrasonic bath for 10 minutes to ensure the dispersion of particles in solution. Then, the solution is maintained under vigorous stirring to ensure stability of the emulsion during the duration of an experiment. An O/W Pickering emulsion is obtained with oil droplets stabilized with fine solid particles. The mean size of the oil droplets is estimated by acquiring images at a framerate of 25 frames per second. Statistics on 10 000 objects shows that 60 % of the oil + solids agglomerates exhibit a diameter lower than 10 µm (See Fig 1S in Supplementary Material).

Table 2. Crude oil characteristics at 1 bar and 293K (14,504 PSI and 67,73 °F)

Characteristics	**Crude Oil**
API density (°API)	21.2
Density (g/cm^3)	0.923
Viscosity (cP)	216

2.2. Porous media

The synthetic porous media are fabricated from a quartz square capillary in which borosilicate beads (38-45 µm) are lightly sintered in order to obtain a 3D consolidated porous medium. A schema with the dimensions are shown in **Fig.1c**. Before filling, both capillaries and borosilicate beads are successively rinsed with Ethanol/Water/Ethanol to remove any traces of organic species on their surfaces. The central part of the quartz capillary is filled with beads. Sintering is then performed under atmospheric conditions in a pre-heated Carbolite AAF calcination oven at a temperature of 1148 K (875 °C) for 10 minutes. Homogeneity and porosity of the porous media are checked by optical microscopy and X-ray microtomography (See Figure 2S in Supplementary Material). A homogeneous repartition of the glass beads all along the porous medium is observed in Figure 2S with a porosity along the z-axis of 43 %. Note that the global porosity of the porous medium is calculated along the z-axis by not considering the first 500 µm of the porous medium where the glass beads are less densely packed. This value of porosity is in agreement with the model of a loose random packing of monodispersed beads packed by hands (Dullien, 1991).

The initial absolute permeability k_0 of the porous medium in its cleanest state is determined with Darcy's law **(Eq.1)** by injecting the clean brine and varying the flow rate from 500 µL/min to 100µL/min and recording the corresponding pressure difference between the inlet and the outlet of the porous medium.

$$\frac{Q}{S} = \frac{k}{\eta L}\Delta P \tag{1}$$

With Q the flow rate, S the cross section of the porous medium, k the permeability, η the fluid viscosity, L the medium length and ΔP the drop pressure.

On more than 50 porous media, the mean initial permeability is evaluated experimentally k_0 = (3.0 ± 0.7) D. The mean porosity, σ = (42 ± 2) % is calculated from the expression (Coelho et al., 1997):

$$k_0 = \frac{\sigma^{5.5} D^2}{5.6} \tag{2}$$

where D is the diameter of the beads, and the mean pore diameter d_p = (14.9 ± 1.4) µm can be calculated from the densely packed uniform spheres model. These experimental findings confirm that the reproducibility of the preparation method is satisfactory.

2.3. Setup description

Fig. 1d depicts our experimental setup that is covered with a black fabric for protection from the ambient light. The porous medium is placed on a XY translation mount in order to adjust its position. The synthetic produced water (noted PW) is injected into the porous medium from either a sealed flask containing the produced water, or a double wall reactor, by using a pressure controller coupled with a flow sensor. A PID feedback loop in between the two devices allows us to continuously monitor the flow rate in the microfluidic setup, by modifying the inlet pressure. Two microfluidic pressure sensors are connected to the inlet and the outlet of the porous medium via three-way valves. To image continuously what occurs in the porous medium during PWRI process, the transparent porous medium is placed in between a set of lights and a camera equipped with a dry microscope objective. For back lighting, we use a white light with a condenser lens behind the porous medium. To obtain a higher definition of the impairment formed during the PWRI injection by backscattering from accumulated solid particles, we place a diffusing light ring in between the sample and the camera.

To enable controlled temperature experiments, the porous medium is placed inside a double wall transparent channel, and the tubes inside sleeves allowing flow of hot water from a heating bath. The temperature difference along the flow line varies within 10 degrees range, and the input temperature is fixed so that it would be 55°C at the output of the porous medium. To minimize temperature loss the flow rate is increased by 2.5 times. Viscosities of the crude oil at 23°C and 55°C are measured in a rheometer and are found to be constant over two decades of shear rates (Fig. 3S). To check whether the variation of permeability with temperature mainly results from viscosity changes, we perform experiments where the crude is replaced with 60/40 Finavestan 50B / crude mixture, having the same viscosity at room temperature as the crude at 55°C (Fig. 3S).

2.4. Experimental procedure

Before any injection experiment, the porous medium is flushed for 30 minutes with CO_2 to prevent air bubbles formation during water filling. The injection circuit (porous medium, pressure sensors and flow sensor) is first filled with filtered distilled water to configure all the devices then with brine. Initial permeability is measured and a global image of the porous medium in its initial state is performed by recombining a set of images acquired all along the porous medium. After this first step, the camera is positioned in front of the porous inlet; the flask containing the PW is connected to the setup and the injection flow rate is imposed at 250 µL/min. We acquire images of the inlet at a framerate of 1 fps for the first 1000 seconds of the injection process and then at 0.1 fps for the last duration of the experiment and record simultaneously the evolution of the inlet and outlet pressures. We determine the injectivity index Ψ from measurements of the pressure drop ΔP(t), along the porous medium accordingly to:

$$\Psi(t) = \frac{k(t)}{k_0} = \frac{\Delta P_0}{\Delta P(t)} \tag{3}$$

with k_0 the initial permeability and ΔP_0 the initial pressure drop. At the end of the PWRI experiment, a global image of the impaired porous medium is captured as previously.

In particular, the spatiotemporal diagrams were calculated by averaging the two-dimensional greyscale maps associated with an image at instant t in the vertical direction y, to obtain the mean greyscale profile at instant t $\bar{g}_t(y) = \langle G_t(x,y)\rangle_x$. These mean profiles are then stacked together vertically in a so-called spatiotemporal diagram (see **Fig. 3b**).

3. Results & Discussion

3.1. Pressure Data

An example of PWRI movie can be seen in Supplementary Material, M1. From the pressure drop data, injectivity indexes Ψ have been plotted versus normalized volumes (i.e. volume/pore volume) known as the injected pore volume (IPV), to monitor the impairment. Injectivity loss is observed and curves from several representative experiments are presented in **Fig. 2.** The superposition of these curves indicates good repeatability at the chosen range of experimental parameters.

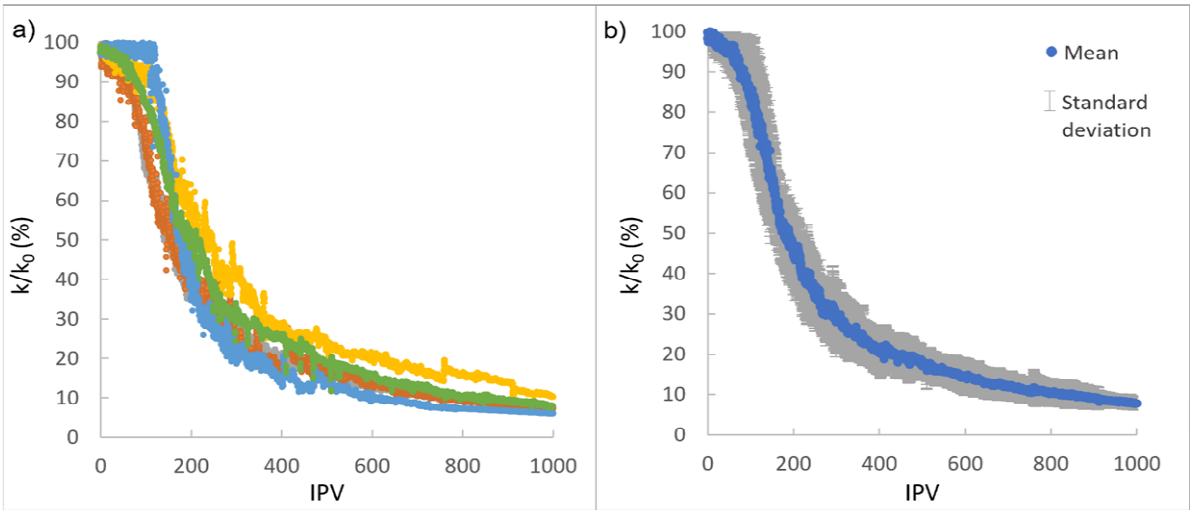

Fig 2. a) Injectivity index versus injected pore volume curves from 5 representative PWRI experiments in 5 porous media with equivalent initial permeability and **b)** the corresponding mean curves with the ±σ boundaries, where σ is the standard deviation at each IPV.

First, an injectivity collapse is observed at the beginning of the injection, then its evolution slows down. A higher pressure drop has to be applied to maintain the flow rate. At the end of the experiment, the PWRI induced a 90-95% injectivity loss of the porous medium. To understand this impairment, we couple these data to direct observations.

3.2. Optical Data

A major advantage of our setup is the porous medium: its transparent composition (quartz capillary and borosilicate beads) is optimal for optical imaging. During PWRI experiments, a series of images of the porous medium inlet was continuously recorded, with an acquisition frame rate of 10 FPS, to highlight the damage kinetics (**Fig. 3a**). Image analysis performed in MATLAB results in spatiotemporal diagrams of light intensity normalized by the intensity in the clean part of the porous medium as function of IPV and position X (with X=0 entrance of the porous medium), as shown in **Fig. 3b.**

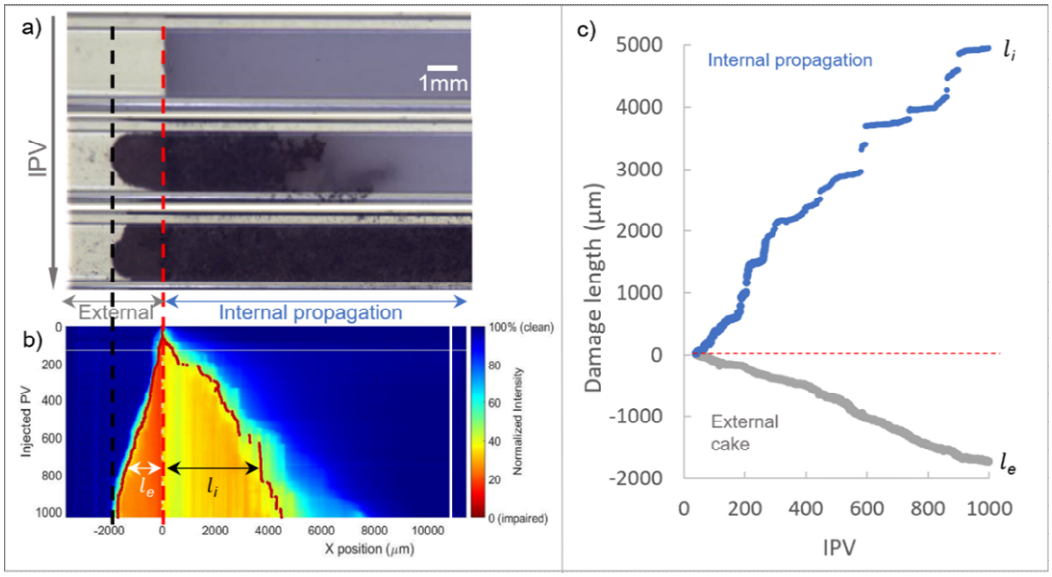

Fig. 3 a) Images of the porous media before (top), during (middle)and after (bottom) PWRI experiment, **b)** the corresponding spatiotemporal diagram, and **c)** Evolution of l_e and l_i from 3b, corresponding to the external and internal damage lengths, respectively.

We point out that the area in front of the porous medium is overexposed during all the images acquisition to improve the resolution in the damaged parts. Therefore, light intensity in this area is underestimated.

From this diagram, we observe that an accumulation of oil and solid particles first occurs at the porous medium entrance (-250 µm < X < +250 µm) at the beginning of the experiment. Then, an external cake forms quickly, before this impairment begins to propagate inside the porous medium. A balance is established between external cake formation and internal propagation: at high IPV, external cake reaches a quasi-stationary size, as shown in the Figure 3b, while the internal damage keeps propagating at quasi-constant mean rate. The mechanism of the external cake stabilization resembles that reported in (Dinh et al., 2020) for a gravitational separator, where the emulsions form a densely packed layer whose thickness reaches a steady state as the coalescence rate is equal to the droplet feeding rate.

For a better understanding of the respective formation kinetics of external cake and of internal damage, a light intensity of 45% corresponding to a "damage threshold" was arbitrarily chosen, above which, position X is still considered clean. All the X positions at this threshold were recorded for each image (i.e., for each IPV) and the damage length L_d is plotted in **Fig. 3c**. L_d mean curve of the 5 representatives experiments, with standard deviation at each IPV, can be found in Fig 4S. Kinetics curves show a linear evolution of the internal damage all along the porous medium during the PWRI experiment while the formation of the external cake gradually tends to stabilize. In some of the experiments, we observe a step like behavior of the propagation of internal damage. We explain this phenomenon as follows: the damage accumulates, the local pressure increases until it reaches a threshold pressure, above which the pressure becomes sufficient to push the damage further inside (Fig.3c). Interestingly, similar behavior was reported in microscale experiments in De Soete thesis (De Soete, 2021) on a single pore scale. These kinetics curves of damage length can be coupled with pressure data for a better understanding of the internal clogging of the porous medium.

3.3. Correlation

We now combine the data obtained from pressure measurements and direct visualizations. On the one hand, a global permeability of the porous medium as a function of IPV was deduced from the pressure drop results (**Fig.2**), with a permeability loss around 90% after PWRI experiment. And on the other hand, the damage kinetics was described thanks to the impairment visualization of the medium (**Fig.3**). Using these two experimental findings, we build a simple model to determine specifically the internal damage permeability k_d.

For this modeling, we do not consider the contribution of the external cake to the overall permeability of the damaged porous medium. Indeed, under the approximation of packed spheres model the permeability scales as D^2 and thus its value is large in the external cake, composed mainly of Pickering droplets. On **Fig. 4a**, three portions of the pressure drop curve are distinguished according to slope differences of linear trends from pressure data (Fig. 2) and optical data (Fig. 3.c). This allows one to determine three regimes: regime 1, 2 and 3 illustrated in **Fig. 5a**. Pressure drops versus damage lengths are also plotted as shown in **Fig. 4b**.

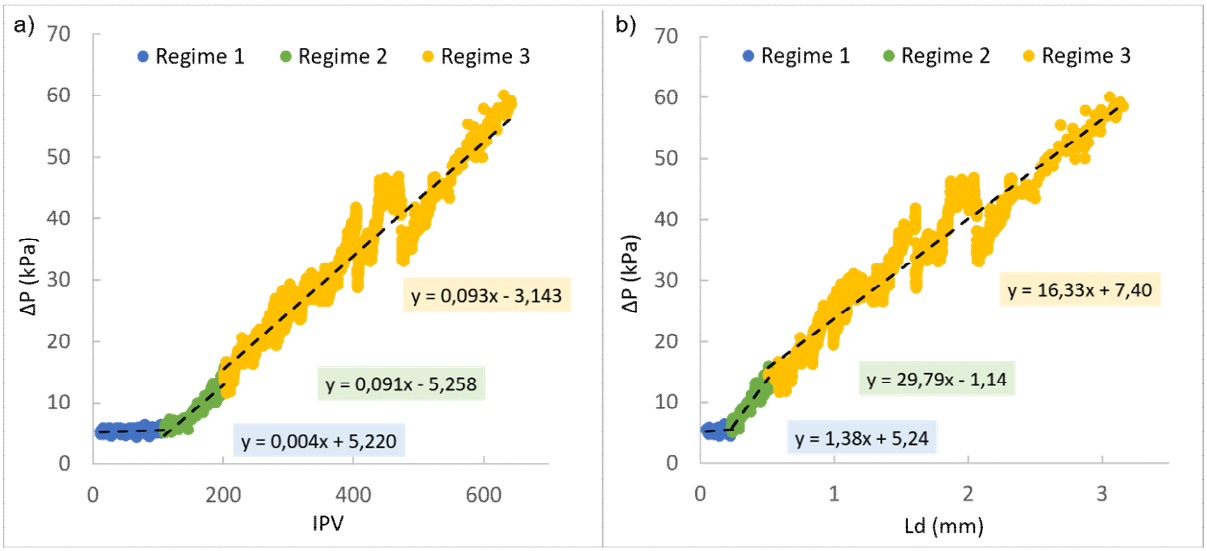

Fig. 4 a) Pressure drop evolution versus injected pore volume and **b)** versus damage length. The equations y=ax+b correspond to the best linear fits obtained for $\Delta P=f(L_d)$ in the three different regions.

Regime 1 corresponds to the rapid accumulation at the entrance to the porous medium at the beginning of PWRI experiment. At this time, the porous medium can be divided into two parts: the first part, close to the entrance, with homogeneous dense damage all along its length. This zone is characterized by a known short length L_{d1} and an intrinsic permeability k_{d1}, different from the bulk permeability k_0. And the second part, a clean one, with a known length L_{c1} and a permeability that equals the initial permeability k_0. Total porous length $L=L_{d1}+L_{c1}$. At this point the damage curve might be sensitive to boundary effects - local heterogeneities stemming from the fabrication process, and subjective definition of the actual entry point by the user (see Fig.2S). Expressing the pressure drop with **Eq.4,** we can calculate k_{d1} from the slope of regime 1 of the $\Delta P=f(L_d)$ curve in **Fig. 4b**:

$$\Delta P(L) = \Delta P(L_{d1}) + \Delta P(L_{c1}) = \left(\frac{\eta Q}{S}\frac{L_{d1}}{k_{d1}}\right) + \left(\frac{\eta Q}{S}\frac{L_{c1}}{k_0}\right) = \frac{\eta Q}{S}\left(\frac{L_{d1}}{k_{d1}} - \frac{L_{d1}}{k_0} + \frac{L}{k_0}\right) \quad (4)$$

Regime 2 corresponds to the growth of the internal dense damage, the porous medium with a damage length L_{d2} is now divided into three parts: the previous dense damaged part from Regime 1 characterized by L_{d1} and k_{d1}, another damaged part which grows more slowly with a length L_{d2}-L_{d1}, and an intrinsic permeability k_{d2}, that could be much lower than k_{d1}, as explained above, and corresponds to the actual damage; and a clean part with a length $L_{c2}<L_{c1}$ with the same permeability k_0. Total porous length $L=L_{d2}+L_{c2}$. Similarly to regime 1, the pressure drop can be expressed by **Eq.5**:

$$\Delta P(L) = \frac{\eta Q}{S}\left(\frac{L_{d1}}{k_{d1}} - \frac{L_{d1}}{k_0} + \frac{L_{d2}-L_{d1}}{k_{d2}} - \frac{L_{d2}-L_{d1}}{k_0} + \frac{L}{k_0}\right) \quad (5)$$

and k_{d2} is calculated with the slope trend of regime 2 from the curve $\Delta P=f(L_d)$ in **Fig. 4b)**.

Regime 3 is related to the deeper damage propagation into the porous media, a critical pressure is reached and a part of the oil separates from the solid particles to propagate alone in the porous media. The porous medium with a damage length L_{d3} is now divided into four parts. Both first parts are defined as previously: first part with a length L_{d1} and a permeability k_{d1}; the second part

with a length L_{d2} - L_{d1} and a permeability k_{d2}. The third part, where the damage is less dense due to oil propagation, has a length L_{d3} - L_{d2} and a permeability $k_{d3}>k_{d2}$. And finally a clean part with a length L_{c3} and a permeability k_0. Total porous length $L=L_{d3}+L_{c3}$. The oil propagation is characterized by formation of the finger pattern (see Movie M1) which indicates formation of preferential paths, a manifestation of the heterogeneous pore size. For this regime, the pressure drop is expressed by **Eq.6**:

$$\Delta P(L) = \frac{\eta Q}{S}\left(\frac{L_{d1}}{k_{d1}} - \frac{L_{d1}}{k_0} + \frac{L_{d2}-L_{d1}}{k_{d2}} - \frac{L_{d2}-L_{d1}}{k_0} + \frac{L_{d3}-L_{d2}}{k_{d3}} - \frac{L_{d3}-L_{d2}}{k_0} + \frac{L}{S}\right) \quad (6)$$

and k_{d3} is calculated with the slope trend of regime 3 from the curve $\Delta P=f(L_d)$ in **Fig. 4b)**. In the case of $k_{d1}=k_{d2}$ regime 1 and 2 can be further simplified into a single regime with a mean permeability k_{d12}.

All the permeability values are reported in **Table 3**.

Table 3. Length and permeability of internal damage for the three regimes of a representative PWRI experiment

Regime	Damage Length (µm)			Permeability (mD)		
Initial	L	18000		k_0	2668	
1	L_{d1}	191	3%	k_{d1}	491	8%
2	L_{d2}- L_{d1}	651	11%	k_{d2}	69	64%
3	L_{d3}- L_{d2}	5363	86%	k_{d3}	104	28%
Final	L_{d3}	6205		k_f	255	

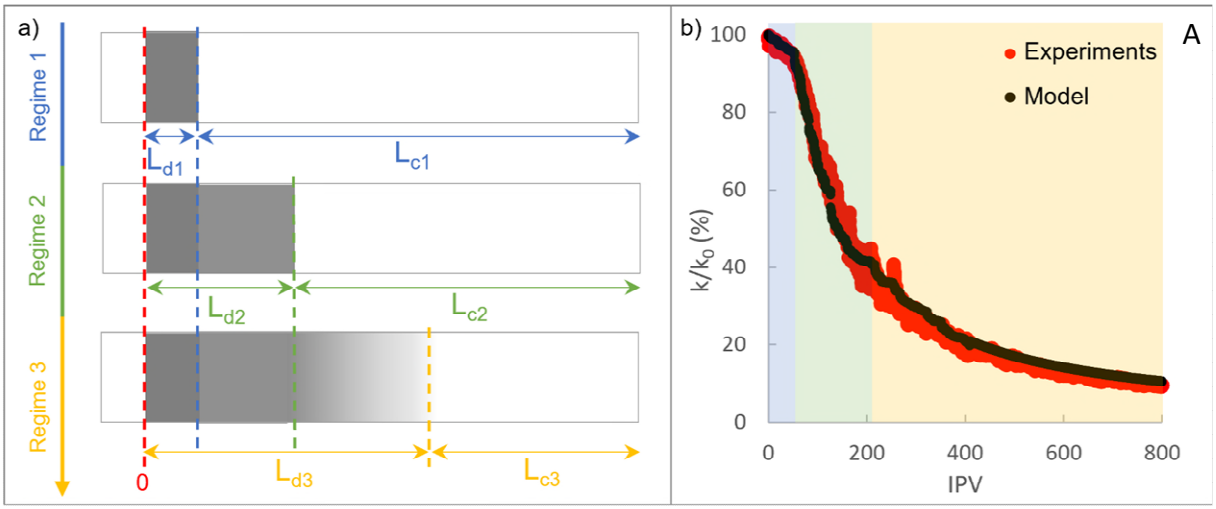

Fig. 5 a) Schema of the porous medium during the 3 different regimes and **b)** theorical and experimental injectivity loss curves versus injected pore volume, for one of the datasets in Fig. 2. The colors on the diagram correspond to the different regimes. The model performs very well also in extrapolation. The extrapolated data is from about 400 IPV, since the images are typically acquired for shorter time compared to the data from the pressure sensors (similarly to **Fig. 5S**).

This model is consistent with our experimental data (**Fig. 5b**) and allows one to highlight this localized damage part with a very low permeability k_{d2} responsible for a major part of the global permeability loss of the porous medium during the PWRI experiment.

3.4. Temperature effect

The following experiments were performed at 71 g/L, 100 ppm solids and 200 ppm oil. To ensure temperature control at the output, the flow rate was increased by a factor 2.5, which had insignificant impact on the damage curves, compared to that of the temperature. The impact of the temperature on the clogging is shown in **Fig.6**. Comparison between the jamming curves on **Fig. 6a** shows that at high temperature the jamming slows down, and it takes more injected volume to achieve the same k/k_0 (alternatively, at a given injected volume, we find ourselves at higher k/k_0). However, a closer look at the snapshots and the spatiotemporal diagrams (**Fig.6b-c**) reveals the important qualitative difference between the two jamming experiments. At higher temperature, the less viscous oil propagates quickly in the porous medium, leaving the particles behind, and the jamming is mainly due to particles. This means that, at the same permeability reduction, a qualitative difference exists between the final jammed states of the two porous media, with higher relative contribution from the jamming due to particles, which cannot be restored with surfactant-based methods. However, at the same injected volume the porous medium at higher temperature was less jammed. The superposition of the jamming curves from experiments with the crude oil at higher temperature and experiments at ambient temperature with the same crude, diluted to have similar viscosity values (**Fig.6d**), implies that the two main mechanisms behind the impact of the temperature on the clogging is a) the lowering of the viscosity and thus

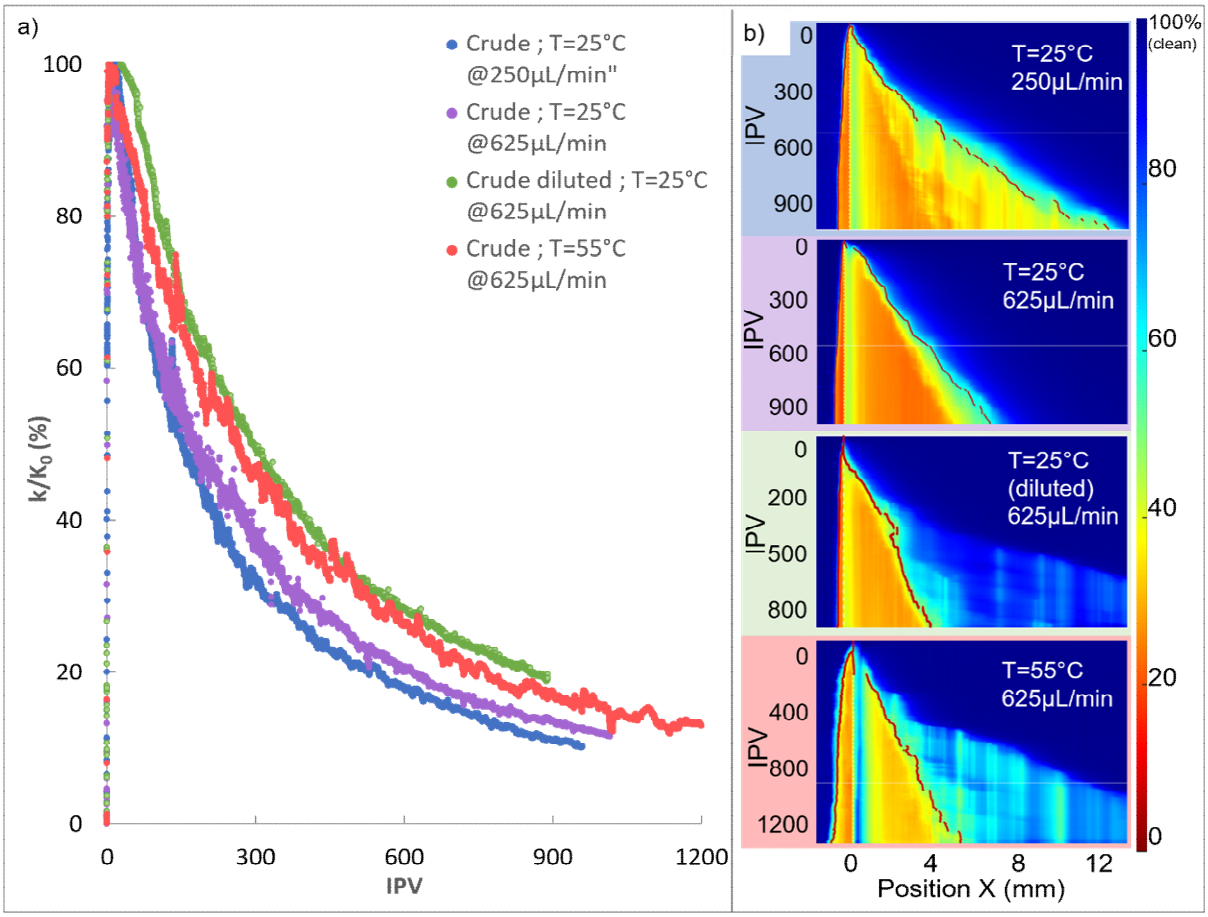

Fig 6. a) Graphic comparing the permeability reduction curves for four different experimental conditions detailed in the inset and **b)** the corresponding spatiotemporal diagrams. The effect of increasing the flowrate is small compared to the temperature effect.

increased mobility of the oil, within the limits of experimental uncertainty, and b) resistance of the Pickering droplets to pressure. At the high temperature (low viscosity) experiment, the spatiotemporal diagrams show rapid spread of oil drops (clear blue), leaving particles behind, which results in particle jamming, that could be irreversible.

4. Conclusions

We presented a novel approach for assessment of damage formation during produced water reinjection. Microscale experimental setup enables rapid assessment and direct observation. The latter in turn enables coupling macroscale measurements with image analysis, resulting in a model for clogging, which is in excellent agreement with the experimental observations. The model divides the porous medium into three regions having different permeabilities at each instant. A small region close to the entrance to the porous medium has significantly smaller permeability and therefore dominates the permeability reduction. As can be seen in Table 1S, the length of the severely jammed region is about 10% of the overall length and it is responsible for over 60% of the injectivity decline (average of 5 experiments).

The mechanisms of the stabilization of the external cake resemble those reported in emulsions and foams, where the steady state thickness is reached when the feeding rate is equal to the disappearance rate, i.e., coalescence in foams/emulsions (Dinh et al., 2020; Tran, 2022) or threshold pressure in Pickering emulsions (De Soete et al., 2021). The growth rate exhibits fluctuations (breathing) due to pressure buildup to a threshold value of the Laplace entry pressure, required to push the droplets through the porous medium, observed also at a single pore level.

Current results imply that temperature impacts the clogging mainly through variation in viscosity but looking at the spatiotemporal diagrams one can see that this requires further exploration with different types of crude oil. At higher temperature we observed an apparent slowdown in the clogging, but the final jam state is qualitatively different, characterized mainly by particle clogging which implies that a) due to the different nature of the damage the model needs to be adjusted to account for the temperature effects, and b) the surfactant-based restoration will be more difficult, as the proportion of the damage due to solid accumulation, and not related to the oil, is more important.

Current work can serve as a starting point for subsequent research. Next the effect of various parameters, such as pore diameter, particle size distributions, multiple size particles / pores, as well as other geometries, can be explored.

Acknowledgements

We thank Helene Berthet for the tomography experiments. We thank Franz De Soete for fruitful discussions. We thank the team of the PIC laboratory in Lacq, in particular Jean-Christophe Aka, for their help with the experiments.

Statements and Declarations

Conflict of interest: The authors declare no conflict of interest.

References

Abou-Sayed, A.S., Zaki, K.S., Wang, G., Sarfare, M.D., Harris, M.H., 2007. Produced Water Management Strategy and Water Injection Best Practices: Design, Performance, and Monitoring. SPE Prod. Oper. 22, 59–68. https://doi.org/10.2118/108238-PA

Agbangla, G.C., Climent, E., Bacchin, P., 2012. Experimental investigation of pore clogging by microparticles: Evidence for a critical flux density of particle yielding arches and deposits. Separation and Purification Technology 101, 42–48 http://dx.doi.org/10.1016/j.seppur.2012.09.011

Ali, M.A.J., Currie, P.K., Salman, M.J., 2007. Permeability Damage due to Water Injection Containing Oil Droplet and Solid Particles at Residual Oil Saturation., in: All Days. Presented at the SPE Middle East Oil and Gas Show and Conference, SPE, Manama, Bahrain, p. SPE-104608-MS. https://doi.org/10.2118/104608-MS

Auset, M., Keller, A.A., 2006. Pore-scale visualization of colloid straining and filtration in saturated porous media using micromodels: Colloid Straining and Filtration. Water Resour. Res. 42. https://doi.org/10.1029/2005WR004639

Azizov, I., Dudek, M., Øye, G., 2021. Emulsions in porous media from the perspective of produced water re-injection – A review. J. Pet. Sci. Eng. 206, 109057. https://doi.org/10.1016/j.petrol.2021.109057

Buret, S.., Nabzar, L.., Jada, A.., 2010. Water Quality and Well Injectivity: Do Residual Oil-in-Water Emulsions Matter? SPE J. 15, 557–568. https://doi.org/10.2118/122060-PA

Buret, S., Nabzar, L., Jada, A., 2008. Emulsion Deposition in Porous Media: Impact on Well Injectivity, in: All Days. Presented at the Europec/EAGE Conference and Exhibition, SPE, Rome, Italy, p. SPE-113821-MS. https://doi.org/10.2118/113821-MS

Coelho, D., Thovert, J.-F., Adler, P.M., 1997. Geometrical and transport properties of random packings of spheres and aspherical particles. Phys. Rev. E 55, 1959–1978. https://doi.org/10.1103/PhysRevE.55.1959

De Soete, F., 2021. Ecoulement de gouttes couvertes dans une contraction. Université Paris Sciences et Lettres.

De Soete, F., Delance, L., Passade-Boupat, N., Levant, M., Verneuil, E., Lequeux, F., Talini, L., 2021. Passage of surfactant-laden and particle-laden drops through a contraction. Phys. Rev. Fluids 6, 093601. https://doi.org/10.1103/PhysRevFluids.6.093601

Delouche, N., Schofield, A.B., Tabuteau, H., 2020. Dynamics of progressive pore clogging by colloidal aggregates. Soft Matter 16, 9899–9907. https://doi.org/10.1039/D0SM01403F

Dinh, H.-H.-Q., Santanach-Carreras, E., Schmitt, V., 2020. Coalescence in concentrated emulsions: Theoretical predictions and comparison with experimental bottle test behaviour. Soft Matter 11. https://dx.doi.org/10.1039/d0sm01459a

Donaldson, E.C., Baker, B.A., Spe-Aime, M., Carroll, H.B., 1977. Particule Transport in Sandstones. SPE 20. https://doi.org/10.2118/6905-MS

Dressaire, E., Sauret, A., 2017. Clogging of microfluidic systems. Soft Matter 13, 37–48. https://doi.org/10.1039/C6SM01879C

Dullien, F., 1991. Porous Media Fluid Transport and Pore Structure, Elsevier Inc. ed.

Evans, R.C., 1994. Developments in Environmental Protection Related to Produced Water Treatments and Disposal (Produced Water Re-Injection). SPE 18. https://doi.org/10.2118/27179-MS

Headen, T.F., Clarke, S.M., Perdigon, A., Meeten, G.H., Sherwood, J.D., Aston, M., 2006. Filtration of deformable emulsion droplets. J. Colloid Interface Sci. 304, 562–565. https://doi.org/10.1016/j.jcis.2006.09.014

Jiao, D., Sharma, M.M., 1993. Mechanism of Cake Buildup in Crossflow Filtration of Colloidal Suspensions. J. Colloid Interface Sci. https://doi.org/10.1006/jcis.1994.1060
Khatib, Z., Verbeek, P., 2003. Water to Value—Produced Water Management for Sustainable Field Development of Mature and Green Fields. SPE 3. https://doi.org/10.2118/0103-0026-JPT
Pang, S., Sharma, M.M., 1997. A Model for Predicting Injectivity Decline in Water-Injection Wells. SPE Form. Eval. 12, 194–201. https://doi.org/10.2118/28489-PA
Rossini, S., Roppoli, G., Mariotti, P., Renna, S., Manotti, M., Viareggio, A., Biassoni, L., 2020. Produced Water Quality Impact on Injection Performance: Predicting Injectivity Decline for Waterflood Design, in: Day 3 Wed, January 15, 2020. Presented at the International Petroleum Technology Conference, IPTC, Dhahran, Kingdom of Saudi Arabia, p. D031S083R001. https://doi.org/10.2523/IPTC-20013-MS
Sauret, A., Somszor, K., Villermaux, E., Dressaire, E., 2018. Growth of clogs in parallel microchannels. Phys. Rev. Fluids 3, 104301. https://doi.org/10.1103/PhysRevFluids.3.104301
Sharma, M.M., Pang, S., 2000. Injectivity Decline in Water-Injection Wells: An Offshore Gulf of Mexico Case Study. SPE Prod Facil. 15, 8. https://doi.org/10.2118/60901-PA
Tran, H.-P., 2022. Moussabilité des Mélanges d'Huiles. Sorbonne Université.
Wyss, H.M., Blair, D.L., Morris, J.F., Stone, H.A., Weitz, H.A., 2006. Mechanism for clogging of microchannels. Physical Review E 74, 061402 https://doi.org/10.1103/PhysRevE.74.061402
Zhang, N.S., Somerville, J.M., Todd, A.C., 1993. An Experimental Investigation of the Formation Damage Caused by Produced Oily Water Injection. SPE 10. https://doi.org/10.2118/26702-MS